Non-Invasive Characterization of the Ionization Region of a Hall Effect Thruster

Ethan T. Dale* and Benjamin A. Jorns†
University of Michigan, Ann Arbor, MI, 48109

The temporal evolution of the ionization region in a magnetically-shielded Hall effect thruster is experimentally characterized. The high-speed changes in size and shape of the ionization region are difficult to quantify non-invasively and may be unreliable when attempted with in situ electrostatic probes. To make these measurements, time-resolved relative ion velocity distributions functions (IVDFs) are acquired non-invasively via laser-induced fluorescence over a large spatial domain. Coupled with downstream probe measurements, moments of the Boltzmann equation taken from these IVDFs are used to compute the ion density, ionization rate, and electric field as a function of time and axial location throughout the domain. This method is performed for an operating condition exhibiting low-frequency "breathing" oscillations, allowing the deformation of the ionization region concurrent with these oscillations to be characterized. Comparisons are made to a previously proposed zero-dimensional model that incorporates one-dimensional ionization region deformation effects to yield unconditional linear growth [1]. It is found that this deformation is experimentally observable but the fundamental zero-dimensional framework of the model is otherwise unrealistic. Alternative factors contributing to the instability are proposed based on the experimental evidence.

I. Nomenclature

c	=	speed of light in vacuum
e	=	fundamental charge
E	=	axial electric field
ℓ	=	neutral decay length
f	=	absolute IVDF
f_0	=	newborn ion IVDF
f_c	=	chopping frequency
f_t	=	trigger frequency
g	=	relative IVDF
j	=	beam current density
L_{iz}	=	ionization region length
m_e	=	electron mass
m_i	=	ion mass
n	=	plasma density
N	=	number of samples
$\dot{n}_0$	=	ionization rate
$n_{n,0}$	=	injected neutral atom density
n_n	=	neutral atom density
T_e	=	electron temperature
T_i	=	ion temperature
$\overline{u^x}$	=	xth velocity moment
u_f	=	ionization front speed
u_i	=	ion speed

*PhD Candidate, Plasmadynamics and Electric Propulsion Laboratory, Department of Aerospace Engineering, Room B107, 1919 Green Road, Ann Arbor, MI 48109.
†Assistant Professor, Co-Director of Plasmadynamics and Electric Propulsion Laboratory, Department of Aerospace Engineering, Room 3037, 1320 Beal Avenue, Ann Arbor, MI 48109, AIAA Senior Member.

u_n = neutral atom speed
α = neutral density ratio
β = neutral-ion length ratio
γ = newborn ion constant
θ = phase
λ = wavelength
μ = Gaussian mean
ν_{iz} = ionization frequency
ξ_{iz} = ionization rate coefficient
σ = Gaussian width
τ = integration time
ω = complex angular frequency

II. Introduction

Hall effect thrusters (HETs) are electric propulsion devices that leverage crossed electric and magnetic fields to efficiently ionize an inert propellant gas and accelerate the resulting quasi-neutral plasma to produce thrust. Although studied for decades, these devices are now quickly becoming a popular solution for near-Earth satellite propulsion due to their high specific impulse compared to chemical systems and moderate thrust-to-power compared to other forms of electric propulsion. HETs are also targeted for deep space applications, where implementing high-power thrusters can enable novel missions [2]. These long-lived (∼10k hours) devices are difficult to test in ground facilities due to facility interactions and the logistical challenges of long duration operation, making self-consistent simulation an integral part of the design and validation process. However, the physics governing the operation of Hall thrusters is still not completely understood. One unclear area is the nature of ubiquitous low-frequency oscillations called the “breathing" mode.

The breathing mode, consisting of ∼10 kHz oscillations in discharge current, has been observed experimentally and numerically for decades [3], yet there is no simple analytical description of this instability that provides intuition into its growth. As there are no non-empirical predictive tools to describe when the breathing mode will onset and what trends it will follow, the oscillatory behavior of a thruster must be experimentally mapped. Studies by Sekerak et al. have shown that the presence of the breathing mode correlates with decreased performance [4]. This lack of understanding is also increasingly becoming a problem in the design and validation of high-power long-lived thrusters as there is evidence of the impact of these oscillations on other important processes, such as pole erosion [5]. Further, recent work [6] has suggested a relationship exists between the breathing mode and anomalous electron transport, another poorly understood aspect of Hall thruster operation.

Previously, the breathing mode has been studied with high-order numerical models that roughly agree with the simple zero-dimensional (0D) predator-prey description of the process put forth by Fife et al. [7]. The breathing mode has been recovered with many simulation schemes, including axial hybrid-PIC [8], axial-radial hybrid-PIC [9], axial-azimuthal full PIC [10], axial fluid [11], and hybrid-direct kinetic [12]. Attempts at analytically describing the growth rate of the instability have either been hindered by intricate analysis that relies somewhat on empirical input [13], or have shown that linear perturbations may be undamped only in unphysical circumstances [14]. It has been shown that introducing self-consistent fluctuations in the length of the ionization region in a simple predator-prey model allows for unconditional growth, although it is unclear if this is a necessary or physically realistic feature [1].

The goals of this work are to establish a method for non-invasively characterizing the shape and extent of the ionization region in a modern HET, and to use this technique to describe how this region changes during a breathing period. Finally, this information will be used to validate the 0D model that predicts growth contingent upon deformation of the ionization region. This paper is organized as follows. First, Section III gives a 0D description of the breathing mode. Then Section IV describes the process of computing the temporally- and spatially-resolved ion density in the ionization region, followed by a review of the experimental setup in Section V. Finally, the raw results are presented and analyzed in Sections VI and VII, respectively, to evaluate the validity of the 0D model.

III. Background

In this paper, we evalute a supposition that allows a 0D model to predict linear growth: the ionization region expands and contracts during a breathing cycle. This model is similar to that proposed by Fife [7], whose results were mirrored by Barral and Ahedo in a different analysis [15]. We assume the ionization region is a 0D box, with neutral particles entering from the anode and exiting to the plume, ions exiting at the beam velocity, and electrons entering from the cathode. In this way, the model excludes radial effects and largely ignores the details of ion acceleration. Within the box, neutrals (prey) are ionized by electrons (predators) to produce ions that are accelerated out. As originally formulated, this model predicts zero growth but experimentally reasonable real frequencies. With corrections proposed by Barral and Ahedo [16] and embraced by Hara et al. [14], the result is similar. The governing equations for this model are expressions of ion continuity and neutral continuity,

$$\frac{dn}{dt} = \xi_{iz} n n_n - \frac{u_i n}{L_{iz}} \tag{1}$$

and

$$\frac{dn_n}{dt} = -\xi_{iz} n n_n - \frac{u_n n_n}{L_{iz}} + \frac{u_n n_{n,0}}{L_{iz}} \quad . \tag{2}$$

Eq. (1) physically states that ion density increases due to ionization and decreases from convection. Eq. (2) conversely states that neutral density decreases due to ionization and increases due to convection.

Although the model of Eqs. 1 and 2 makes intuitive sense, it provides no insight into the energy source for this instability. It has been shown that including perturbations in u_i and ξ_{iz} (via T_e) does not make the model unstable [1]. The only remaining quantity that may vary significantly is the ionization region length L_{iz}, and thus there is a need to model changes in ionization region length due to changes in ion and neutral density. To do this, we assume the ionization region is an isolated block of plasma, where the upstream edge (“ionization front") is a transition from pure neutral gas to a mixture of ions and neutrals. This is depicted in Fig. 1, where there is a front that merges into a region of constant ion density that eventually accelerates out of the thruster. Neutral continuity in the frame of reference of the ionization edge yields the ionization front velocity, Eq. (3). The non-Galilean transformation required to obtain this form is described in [1].

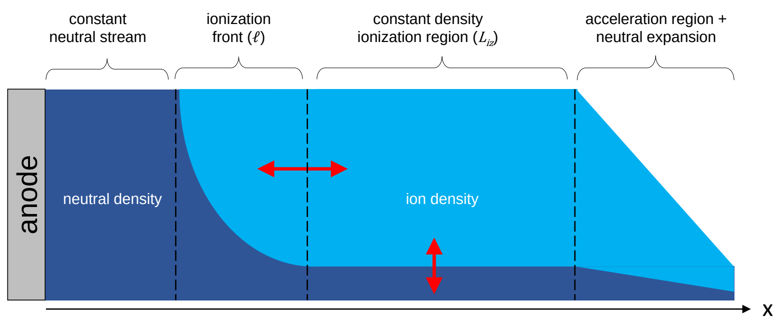

Fig. 1 An illustration of the physical setup for modeling changes in the ionization region length, in which an ionization front is modeled. The red arrows indicate the assumed fluctuations in this model, i.e. the ion density in the ionization region and the location of the ionization front.

$$u_f = u_n - n\xi_{iz} n_n \left(\frac{\partial n_n}{\partial x}\right)^{-1} \approx u_n - n\xi\ell \tag{3}$$

The ionization length can be described as

$$L_{iz} = L_{iz,0} - \int u_f dt = L_{iz,0} + \int n' \xi_{iz} \ell dt = L_{iz,0} + i\frac{\xi_{iz}\ell}{2\omega} n' \quad , \tag{4}$$

where it is assumed that small perturbations in plasma density are sinusoidal in time such that $n = n_0 + n'$ where $n' = \tilde{n}\exp(-i\omega t)$ and $\tilde{n}$ is the small oscillation amplitude. In the steady state, $u_f = 0$ and $u_n - \ell n_0 \xi_{iz} = 0$. Physically, this equation implies that changes in the ionization region length lag behind changes in ion density by 90°. In a linear sense, perturbations in the inverse of L_{iz} lead changes in n by 90°. Qualitatively, this can be understood as the ionization region stretching or compressing in response to variations in bulk ion density, with a lag occurring due to the inertia of the front. This lag represents a possible energy source for the instability.

The linearized system of Eqs. (2), (1), and (4) forms a matrix equation whose determinant yields an expression for the complex perturbation frequency, ω. The imaginary part of ω is the growth rate, which is effectively an analytical description of the driving force behind this instability. The determinant is

$$i(\alpha-1)\beta u_i u_n^2 + (\alpha-1)(\beta-1)L_{iz}u_i u_n\omega + i\alpha L_{iz}^2 u_n\omega^2 + L_{iz}^3\omega^3 = 0 \quad , \tag{5}$$

where $\alpha \equiv n_{n,0}/n_n$ and $\beta \equiv \ell/L_{iz}$ for simplicity. An exact analytical form for the roots of ω exists but is much too complicated to be useful for judging the stability of the system, but applying the Routh-Hurwitz theorem [17] provides the following criteria for stability:

$$-\frac{(\alpha-1)\beta u_i u_n^2}{L_{iz}^3} > 0 \tag{6}$$

$$\frac{\alpha u_n}{L_{iz}} > 0 \tag{7}$$

$$\frac{(\alpha-1)u_i u_n^2(\alpha(\beta-1)-\beta)}{L_{iz}^3} > 0 \quad . \tag{8}$$

Given that the ratio of injected neutral density to the density inside the box is greater than unity, $\alpha > 1$, and the ratio of the neutral decay length to the ionization region length is positive, $\beta > 0$, these criteria cannot be satisfied and thus the system is always unstable. In total, including deformation of the ionization region is sufficient for purely growing linear perturbations in this simple 0D system.

Physically, the lag between perturbations in ionization region length and ion density allows for growth of these perturbations. As density increases, the ionization region broadens, which tends to slow the rate of change of density. But because this broadening lags, there is a portion of the breathing cycle during which the density is decreasing both due to predator-prey processes and due to broadening of the ionization region. In some sense, the energy for the perturbation is coming from the additional volume of neutrals being consumed by the ionization region as this region deforms. This drives the breathing mode, allowing it to grow until it nonlinearly saturates.

The preceding description of the breathing mode assumes that the ionization region stretches and compresses with a lag compared to fluctuations in ion density. The success of this model therefore hinges on the experimental observation of this behavior. Given that the model assumes the ionization region can be delineated from the ion density profile throughout the channel, ion density must be measured as a function of time and the following observations must be made to validate the model:

I. *Correlation*: Ion density and ionization region width fluctuations correlate with breathing as identified via discharge current fluctuations.
II. *Zero-dimensionality*: Ion density fluctuations throughout the ionization region are in phase.
III. *Quadrature*: Ionization region width fluctuations lag ion density fluctuations.

IV. Methodology

The primary measurement we make in this study is temporally- and spatially-resolved ion density inside the thruster channel. Time-averaged density measurements have been made in this region before, and time-resolved density maps have been measured in other regions. However, the measurements involved in the present study are unprecedented. First, we review previous techniques for making similar measurements, and then we discuss an alternative approach.

A. Existing Diagnostic Techniques

Density measurements have been made inside a HET before using a rapidly reciprocated electrostatic probe. For instance, Haas injected a Langmuir probe into a 5-kW Hall thruster and generated profiles for density, temperature, and plasma potential [19]. Lobbia et al. have performed considerable work on operating high-speed Langmuir probes in electric propulsion plasmas [20] and successfully applied them to HET plumes [21], but attempts to probe closer to the thruster have led to irreconcilable perturbation of the thruster and were met with severe limitations imposed by the probe electronics [22]. Work by Jorns et al. [23] and Grimaud et al. [24] has highlighted the perturbative effect of near-field in situ probing. Although the perturbation can be minimized, it is difficult to verify that the measurements being made are representative of the “natural" operation of the device without extensive verification with less invasive diagnostics like laser-induced fluorescence (LIF) or planar probes mounted flush with the channel walls.

LIF is commonly used to measure the time-averaged and time-resolved ion velocity distribution function (IVDF) in HETs. It can also be used to estimate the electric field by characterizing the change in beam velocity at different points in space. Measurements can be made inside the thruster by injecting and collecting light at an angle, and in fact the edge of the anode presheath (where there is no bulk ion motion) can be probed [25]. This is especially easy for magnetically-shielded thrusters which generally have discharges pushed downstream due to their unique magnetic field topography [26]. Time-resolved LIF (TRLIF) measurements have shown considerable changes in the IVDF during a breathing cycle, with the most probable ion velocity varying drastically [27, 28]. This suggests that the electric field is changing shape and/or peak location during breathing, which is supported by simulations [8]. However, LIF does not readily yield absolute densities, nor are absolute intensities measured at different locations directly comparable. Alternatively, one of the few non-invasive techniques for measuring absolute densities is microwave interferometry[29] but it is unclear that it could be performed sufficiently upstream of the acceleration region and with sufficient spatial resolution to be useful.

B. Proposed Technique

1. Theory

The one-dimensional Boltzmann equation,

$$\frac{\partial f}{\partial t} + u\frac{\partial f}{\partial x} + \frac{e}{m}E\frac{\partial f}{\partial u} = \nu_{iz} f_0 \quad , \tag{9}$$

can be used to compute the electric field E and ionization frequency ν_{iz} for low-temperature plasmas including electric propulsion plasmas, as demonstrated by Perez-Luna et al. [30]. In the formulation of Eq. (9), ionization is included as the product of the ionization frequency and the newborn ion IVDF f_0, and other collisions are ignored. This assumption is reasonable for a Hall thruster where ions tend to move ballistically: the ion transit time is much smaller than the ion collision time. The one-dimensional assumption also implies that there is little variation in ion properties across the width of the plasma and that there is little divergence of the ion beam. The latter assumption is fair close to the acceleration region. LIF directly produces a reasonable estimate of the normalized IVDF, $g \equiv f/n$, such that the Boltzmann equation establishes the relationship between LIF measurements and ion density. In the work of Perez-Luna et al., the time-averaged Boltzmann equation loses its dependence on density, so only g had to be measured. In this paper, we apply this method to a time-varying plasma, so the relationship between LIF measurements and density is preserved. This provides an opportunity to compute density given a map of TRLIF measurements

The zeroth, first, and second velocity moments of the Boltzmann equation are computed as

$$\frac{\partial n}{\partial t} + \overline{u}\frac{\partial \overline{u}n}{\partial x} = \dot{n}_0 \quad , \tag{10}$$

$$\frac{\partial \overline{u}n}{\partial t} + \frac{\partial \overline{u^2}n}{\partial x} - \frac{e}{m}nE = 0 \quad , \tag{11}$$

and

$$\frac{\partial \overline{u^2}n}{\partial t} + \frac{\partial \overline{u^3}n}{\partial x} - 2\frac{e}{m}nE = 3\frac{e}{m}T_i\dot{n}_0 \quad . \tag{12}$$

These equations are expressions of continuity, momentum conservation, and energy conservation, respectively, where the only applied force is due to the electric field, and ionization acts as an energy source. Fluid codes utilize these equations and their electron counterparts to self-consistently determine electric field, ionization rate, and density. But following the Perez-Luna method, if all moments of the relative IVDF are known and $n(t)$ is known, the quantities $\dot{n}_0$, $\partial n/\partial x$, and E can be solved for explicitly. Eq. 13 gives the solution for $\dot{n}_0$ where γ is a constant related to newborn ions, and Eqs. 14 and 15 give $\partial n/\partial x$ and E in terms of $\dot{n}_0$. As Eq. 13 shows, the newborn ion temperature T_i must also be known. For typical low-temperature electric propulsion plasmas, the ions are much colder than the electrons; in Hall thrusters, the electron temperature is typically at most ~10 eV, and so in this study it was reasonable to assume $T_i \sim 0.1$ eV. Although T_i can be estimated from g, the calculations of Eqs. 13-15 are typically insensitive to the exact value of T_i.

$$\dot{n}_0 = \frac{u(-2u(\frac{\partial n}{\partial t}u + n(\frac{\partial \overline{u^2}}{\partial x} + \frac{\partial u}{\partial t})) + \overline{u^2}(3\frac{\partial n}{\partial t} + 2(\frac{\partial \overline{u}}{\partial x}n) + (\frac{\partial \overline{u^2}}{\partial t}n + (\frac{\partial \overline{u^3}}{\partial x}n) - \overline{u^3}(\frac{\partial n}{\partial t} + \frac{\partial \overline{u}}{\partial x}n)}{3\gamma\overline{u} + 2\overline{u}\overline{u^2} - \overline{u^3}} \tag{13}$$

$$\frac{\partial n}{\partial x} = \frac{\frac{\partial n}{\partial t} + n\frac{\partial \overline{u}}{\partial x} - \dot{n}_0}{\overline{u}} \tag{14}$$

$$E = \frac{e}{m}\left(\frac{(\overline{u^2} - \overline{u}^2)\frac{\partial n}{\partial t} + n\overline{u^2}\frac{\partial \overline{u}}{\partial x} - n\overline{u}\frac{\partial \overline{u^2}}{\partial x} - n\overline{u}\frac{\partial u}{\partial t} - \overline{u^2}\dot{n}_0}{n\overline{u}}\right) \tag{15}$$

As Eqs. (13) to (15) show, only the first and second velocity moments are needed to compute $\partial n/\partial x$ and E. However, $\overline{u^3}$ and its gradient is required to determine $\dot{n}_0$. Measured g will always contain noise, which easily leads to inaccurate estimates of higher order mean velocities. As a result, Eq. (13) may need to be simplified using estimates of $\overline{u^3}$ that rely on lower order mean velocities. It can be shown that the approximation $\overline{u^3} \approx \overline{u}\overline{u^2}$ yields an error of $2\sigma^2/(\mu^2 + 3\sigma^2)$ for a Gaussian IVDF of mean μ and width σ. In a Hall thruster, downstream of the acceleration region this error becomes small, $\mu \gg \sigma$, and upstream it amounts to at most 67%. It can similarly be shown that the approximation $\overline{u^3} \approx \overline{u}^3$ has only 1.5 times greater error.

Of the quantities $\dot{n}_0$, $\partial n/\partial x$, and E, any two can be expressed as a function of the third. In this formulation, $\dot{n}_0$ is chosen as the independent quantity because it is the only one with a clear physical limit that can be used to identify when an approximation for $\overline{u^3}$ is required: $\dot{n}_0$ cannot be negative. The electric field could be used in a similar capacity because time-averaged measurements in typical HETs show it to be positive along channel centerline, but it is not known a priori whether the electric field momentarily reverses at certain locations and phases during a breathing cycle.

In summary, Eqs. (13) to (15) can be used to estimate the ionization rate, electric field, and density gradient over some domain given $n(t)$ at a point and $g(u, x, t)$ everywhere in the domain. The latter quantity is yielded by spatial and temporal IVDF measurements via TRLIF. The former quantity is required as a boundary condition for the Boltzmann equation moments, and thus the practical application of this method where these measurements are combined must also be discussed.

2. *Practical Approach*

The practical goal of this technique is to determine ion density temporally and spatially in regions of the thruster inaccessible with in situ probes. The equations of the previous section indicate that, given a map of TRLIF measurements, the local density at each point in space and time can be used to determine the density gradient everywhere. Alternatively, if $n(t)$ is determined at a single location using an electrostatic probe, and Δx is the TRLIF map spatial resolution at that point, the gradient at that location can be computed and thereby the density at nearby points estimated in the following way:

$$n_{i-1} = n_i + \int_{x_i - \Delta x}^{x_i} \frac{\partial n}{\partial x} dx \approx n_i - \left(\frac{\partial n}{\partial x}\right)_i \Delta x_i \quad . \tag{16}$$

This process can then be repeated over the entire spatial range of TRLIF measurements. The result will be a temporal and spatial map of ion density extending far beyond the useful range of the electrostatic probe used to determine the boundary value of $n(t)$. Put another way, Eqs. (10)-(12) define a system of partial differential equations that can be solved numerically given boundary conditions on n and $\partial n/\partial t$.

To summarize, the practical steps for this technique are as follows:

1) Acquire TRLIF measurements over a wide spatial range.
2) Measure time-resolved current density with a Faraday probe at the most downstream (non-perturbative) point in the TRLIF measurement domain.
3) Compute $n(t)$ at the Faraday probe location via $n(t) = j(t)/\overline{u}(t)$, where $\overline{u}$ comes from the coincident TRLIF measurement.
4) Compute $\partial n/\partial x$ using Eqs. (13)-(15).
5) Compute the density at the next upstream point in the TRLIF map via Eq. (16).
6) Repeat until $n(t)$ has been computed over the entire TRLIF spatial domain.

3. Limitations

We rely on many assumptions for the success of this technique. First, as mentioned previously, determining moments of the IVDF can be difficult for a noisy fluorescence signal. This is particularly challenging for TRLIF measurements, where the signal-to-noise (SNR) is often especially low compared to time-averaged LIF. Section V C will provide examples of this effect. Compensating for inaccurate IVDF moments can be tackled in two ways: algorithmically increasing SNR of the measured LIF data, and applying approximations for higher moments. The first approach can be achieved with various techniques, such as Saviztky-Golay smoothing or least-squares Gaussian fitting. The former may not eliminate noise at high velocities sufficiently to improve moment calculations, and the latter may still skew moment calculations slightly by misrepresenting the IVDF shape. Sometimes the Gaussian fit can be used to define edges of the IVDF beyond which noise can be subtracted, but determining those edges can be somewhat arbitrary. An alternative approach we use is to fit a Gaussian to the measured data and then normalize the product of the raw data and this fit. This effectively eliminates noise in the wings of the IVDF but also retains strong non-Gaussian features elsewhere, although it is still not a perfect representation of the raw data.

Another limitation of this technique is that the fidelity of the resulting density map depends on the temporal and spatial resolution of the TRLIF data. Poor temporal resolution will lead to inaccurate estimates of $\partial n/\partial t$ and the rates of change of the mean velocities, which then leads to inaccurate $\partial n/\partial x$. Poor spatial resolution will lead to inaccurate estimates of $n(t)$ as it is iteratively computed throughout the TRLIF domain. Linearly interpolating the measured quantities spatially can improve the precision of the $n(t)$ estimates but does not guarantee improved accuracy. Higher-order integration schemes can improve the fidelity of the $n(t)$ calculation but anecdotally the practical spatial resolution afforded by the TRLIF setup in this experiment is coarse enough that these more complicated schemes do not greatly change $n(t)$. On the contrary, these schemes will often make $\dot{n}_0$ more sensitive to higher-order mean velocities, potentially leading to less accurate predictions of density. For that reason, we empltoy simple trapezoidal integration when analyzing the data.

A final limitation is the time sensitivity of this method and the implications for estimating ion density. Time-averaged LIF traces often show “smeared" IVDFs: g may be saddle-shaped or even appear to be composed of two separate Gaussian distributions. This smearing may be a result of oscillations in the IVDF faster than the integration time of the fluorescence detector. However, the average of the moments of a time-resolved IVDF will not necessarily equal the moments of the time-averaged IVDF depending on the frequency of the smeared oscillations, so this smearing ultimately may skew estimates of E, $\partial n/\partial x$, and $\dot{n}_0$. Although the most significant oscillations in a Hall thruster are often due to the breathing mode, there is also non-negligible power at higher frequencies, and occasionally there are coherent modes to be found at these frequencies. As a result, even TRLIF measurements aimed at recovering breathing oscillations may measure smeared IVDFs. Section VI C will show that we indeed measured smeared IVDFs during the experiment described in this paper. Although possibly coincidental, it is noteworthy that increasingly worse approximations of $\overline{u^3}$, such as $\bar{u}\overline{u^2}$, were required such that $\dot{n}_0$ remained positive in the region where this smearing was observed, indicating that the calculated $\overline{u^3}$ – and thus the measured IVDFs – in this region may have been inaccurate.

V. Experimental Setup

Now that we have described the theoretical and practical implementation of the proposed method, the experimental approach for this study will be discussed. This includes a review of the facility, thruster, and diagnostic apparatus required to perform the desired ion density measurements needed to validate the 0D model. As reviewed in the previous section, a Faraday probe provides the ion density boundary condition far downstream, and TRLIF maps are applied to moments of the Boltzmann equation to deduce density upstream of this boundary.

A. Facility and Thruster

This experiment was conducted at the Plasmadynamics and Electric Propulsion Laboratory of the University of Michigan in the Large Vacuum Test Facility (LVTF), a 9-meter long, 6-meter diameter stainless steel-clad chamber. The facility was undergoing upgrades involving new pump installation during the course of this study, but all data was taken with the chamber pumped to high vacuum with eight LN_2-baffled TM-1200 cryogenic pumps, and additionally pumped during thruster operation with five copper cryogenic “thumpers". The total pumping speed for this experiment was approximately 300 kL/s on xenon in this configuration. Pressure in the chamber is measured with a MKS 370 Stabil-Ion gauge, located in the exit plane of the thruster and approximately 1 m away from thruster centerline, as recommended by Dankanich et al. [31]. Gas is supplied to the thruster with two Alicat MC series mass flow controllers fed with

99.9995% pure xenon.

The H9, a 9-kW magnetically-shielded Hall thruster developed jointly by the University of Michigan, the Jet Propulsion Laboratory, and the Air Force Research Laboratory, was the subject of this study. Its design and performance have been described elsewhere by Hofer and Cusson et al. [32, 33]. Photos of the thruster after manufacture and installed in the chamber are shown in Fig. 2. The thruster was paired with a lanthanum hexaboride hollow cathode mounted centrally and operated with a nominal 7% flow fraction. All data was taken with nominal magnetic field settings in a naturally oscillatory mode at 300 V, 2.5 kW. At this condition, the facility pressure was approximately 4 μTorr-Xe. The body of the thruster was electrically isolated from the facility and tied to the cathode during operation.

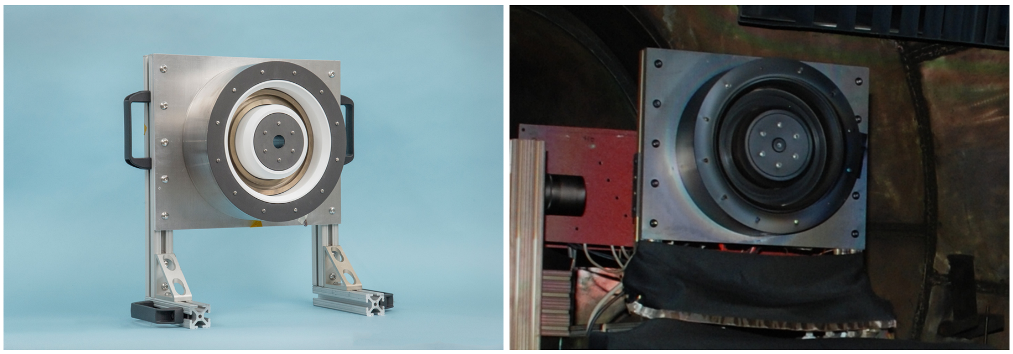

Fig. 2 The H9 before any testing (left) and installed in LVTF (right). The channel ceramics were coated with graphite due to prior testing. This coating is a qualitative indication of effective magnetic shielding.

B. Faraday Probe Setup

Current density measurements were performed 35 mm downstream of the thruster exit plane with an unguarded planar probe, pictured in Fig. 3. The collector was a 4.8 mm^2 graphite rod housed in alumina. The probe was sized for a thin sheath while drawing very little total current and occluding very little of the total plume area. The probe was axially injected toward the thruster at 50 cm/s using a 2-m long ironless linear motor. The total residence time of the probe at its measurement point was less than 1 s, and no major changes in discharge current or oscillation amplitude were observed during this time. Likewise, the current collected from the probe showed no discernible trend throughout the acquisition, indicating that probe heating effects were minimal.

The Faraday probe generally collected ~1 mA of DC current, as was expected from the probe dimensions and the typical near-field beam current density for the H9. When trying to resolve breathing oscillations, even smaller signals must be measurable to achieve good temporal resolution. Increasing the signal gain with a large shunt resistor will inevitably lead to reactive current that distorts high-speed signals, especially when trying to acquire at ~100 MS/s to provide as many current samples as possible. For this experiment, a DC supply biased the collector to -25 V and voltage was measured from ground across a 1 Ω shunt resistor into an Alazar 9462 digitizer. The discharge current as measured with a Tektronix TCP312A split-core current probe and TCPA300 amplifier was simultaneously measured with the same digitizer. As expected, the raw current signal was drowned with high-frequency noise but by acquiring over many breathing periods a clean average signal was recovered.

C. TRLIF Setup

1. Theory

Laser-induced fluorescence is a common technique in diagnosing electric propulsion plasmas [25]. LIF involves exciting a specific Xe II transition in a plasma plume and measuring the light fluoresced as a result of that transition. For this experiment, the non-resonant $5d[4]_{7/2}$ - $6p[3]_{5/2}$ transition was exploited, where the nominal transition wavelength in vacuum is 834.953 nm and the fluorescence wavelength is 542.1 nm. It is assumed the targeted metastable population for this transition is representative of the ground Xe II population. When the laser is detuned from the excitation wavelength, some ions will still excite due to Doppler shifting as follows:

$$\Delta\lambda = \lambda_{tr}\left(\frac{u_i}{c}\right) \quad . \tag{17}$$

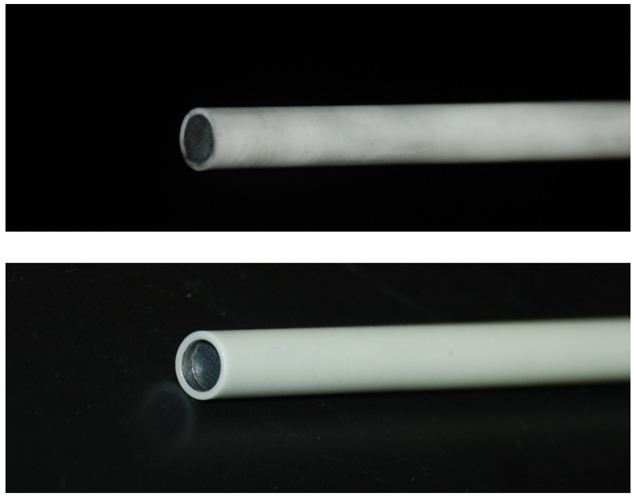

Fig. 3 **The Faraday probe used for beam current density measurements in this experiment, before testing (top) and after (bottom). The collector eroded significantly over roughly twenty hours of testing, but all measurements for this experiment were made within the first hour.**

As Eq. 17 shows, the detuning increment $\Delta\lambda$ can be related to the ion velocity. If fluorescence intensity is measured over a range of detuned wavelengths, the relative density of ions as a function of velocity is in effect measured. However, there are many subtle effects that can complicate this technique, such as natural line broadening, Zeeman splitting, and excitation saturation. The uncertainty due to many of these effects is small and symmetric, so they are ignored in this experiment. Using the approaches of Huang et al. [34] and Jorns et al. [35], and assuming Gaussian IVDFs, we estimate the Zeeman splitting to contribute <10% uncertainty to $\overline{u^2}$ and $\overline{u^3}$ at all times within the entire TRLIF domain, <1% at the exit plane, and even less downstream. Saturation was evaluated in a time-averaged sense at a single operating condition and a single spatial point. It was found that saturation was negligible at the laser power level for which the data in this experiment was taken.

In LIF applications, the fluorescence signal is often much weaker than the total collected light, so homodyning is often used to detect it. Commonly, the injected light is modulated and a lock-in amplifier (LIA) filters the signal to yield the modulated (fluorescence) component. When modulating with a mechanical chopper, a reasonable upper limit on the chopping frequency f_c is 10 kHz. For the homodyning to work, the LIA integration time τ must be much greater than $1/f_c$. This generally means that integration times above 100 ms are required, implying that this technique can only detect fluctuations around 5 Hz or slower. To allow LIF measurements of the breathing mode without fundamentally changing this detection method, we used a boxcar averaging scheme [28]. This method utilizes a gating circuit to precisely sample the fluorescence signal at a given delay from a known phase in the breathing cycle. The signal produced by the gating circuit is fed into the lock-in amplifier as before but now the fluorescence signal filtered out by the LIA pertains to a specific phase of the breathing cycle. If the gate delay is varied, an entire cycle can be measured, in effect producing a time-resolved LIF measurement. The laser modulation must be much slower than the trigger frequency of the gating circuit, and both must be faster than the integration frequency of the lock-in amplifier. In most cases the discharge current is the sensible choice for triggering the gating circuit. Occasionally the discharge is forced to oscillate to produce sufficiently coherent discharge current fluctuations[36] but that was not necessary in this study.

2. Time-Averaged Setup

Figure 4 shows a diagram of the typical time-averaged LIF setup that serves as the backbone of the TRLIF measurements made in this experiment. First the laser is sampled to determine its wavelength and intensity, as well as directing it to an optogalvanic cell for a nominal transition wavelength reference. The signal is then split and chopped at distinct frequencies between 1 and 5 kHz, allowing the interrogation of two independent signals simultaneously. The signal is fiber-coupled and focused to a $\sim$1 mm^3 point along the thruster axial direction using an achromatic doublet lens. In the transverse direction, the interrogation point was located at thruster channel centerline. The thruster was mounted on a motion stage for axial repositioning. In this experiment, measurements were made from 25 mm upstream to 35 mm downstream of the exit plane (conventionally, -25 mm to 35 mm). The injection optic was positioned approximately 2 m downstream of the thruster. Figure 5 is a photograph of this setup. The optic was mounted on a 2D fine translation stage to maintain alignment as it and its mounting hardware heated up in the thruster plume during testing. The collection optics consisted of a collimating lens at the front of the lens tube and a focusing lens at the back of the tube. This allowed light to be collected close to the thruster while keeping the mounting hardware and fiber far away, which is critical for configurations that allow optical access deep inside the thruster channel. The collected light is filtered through a spectrometer and sent into a photomultiplier tube, which outputs current to a trans-impedance amplifier (TIA). The resulting voltage signal is fed into a lock-in amplifier.

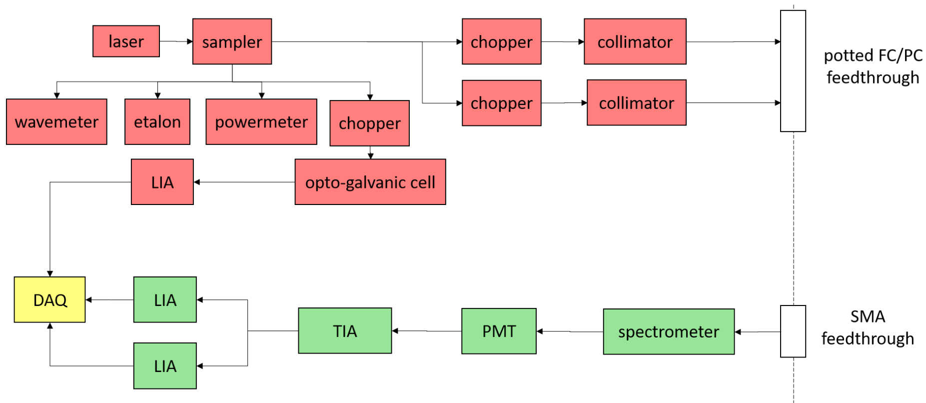

Fig. 4 The architecture of a typical time-averaged LIF setup, consisting of an injection (red) branch and a collection (green) branch. In this experiment, only minor modifications were made to this setup to allow TRLIF measurements.

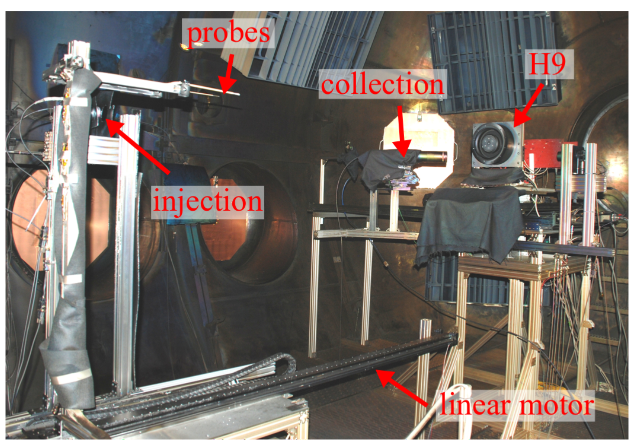

Fig. 5 The internal LIF setup, showing the injection mount and probe stand on the left, and the collection optics and thruster on the right.

3. Time-Resolved Setup

The boxcar averaging setup we used was comprised of a custom trigger circuit, a SRS SR250 gated integrator, and a SRS SR245 computer interface. In the context of Fig. 4, the gated integrator was placed ahead of one of the collection lock-in amplifiers. This meant that one LIA was sampling the fluorescence at a specific phase, while the other LIA was sampling the time-averaged fluorescence. This was done to ensure that the time-averaged signal was not varying greatly during the lengthy time-resolved acquisition. The gated integrator was set to integrate over 10 μs – establishing a Nyquist frequency of 50 kHz – and the delay was controlled by the SR245 with 10-bit resolution between 0 and 600 μs. The breathing oscillations in this study almost universally had a period of 65 μs, so only a fraction of this delay range was used. The SR250 was found to trigger irregularly above 10 kHz at the operating condition of interest, so the trigger rate was limited to 5 kHz for reliability. To do this, the trigger circuit included not only a comparator for detecting when a preset trigger voltage was exceeded but also a monostable timer to produce a TTL pulse of constant 200 μs width. For each TRLIF acquisition, 100 ms of the discharge current waveform was recorded with a Keysight DSOX3024A oscilloscope using the same current sensing hardware as in the Faraday probe setup.

Several aspects of this setup should be noted before exploring the data produced with it. First, the SR250 is capable of producing a running average of up to ten thousand samples, but for this averaging to be effective the following condition must be met: $N f_c \ll f_t$. That is, each “chop" must encompass many times the number of integrator samples to be averaged, otherwise the averaging will attenuate the fluorescence signal. For the sake of reliability and simplicity in this experiment, the trigger frequency was kept lower than necessary and no averaging was used, requiring a 500 Hz chopping frequency for satisfactory SNR. A lower f_c would improve the quality of the signal coming out of the integrator but reduce the quality from the LIA, while the reverse is true for a higher f_c.

Second, it should be expected that the SNR will degrade for longer delays. Because breathing oscillations are commonly broadband, discharge current fluctuations often vary somewhat in amplitude and period cycle-to-cycle. When triggering from a zero crossing in the discharge current, longer delays allow more time for the cycles to deviate, which results in a noisier LIF trace. Although triggering from a non-zero discharge current may help eliminate noise from mistaken triggering off of weaker high-frequency oscillations, it can also introduce noise evenly across all delays. For this reason, we chose the trigger level to be the discharge current zero crossing for this experiment.

VI. Results

A. Discharge current

Figure 6 shows a sample of the raw cathode current as well as an average cycle. The average signal is downsampled to match the temporal resolution of the TRLIF measurements. Also note that the last point of the signal is at a phase greater than 360°, again to match the phases of the TRLIF measurements. Figure 7 shows the power spectra of the discharge current during a TRLIF acquisition and during a Faraday probe acquisition, which were performed sequentially rather than simultaneously. As expected, most power resides in low frequencies. Both spectra have a defined low frequency peak, although the TRLIF peak is at 15.4 kHz and the Faraday probe peak is at 11.5 kHz. In fact, all TRLIF acquisitions had a peak near 15.2-15.6 kHz, while all Faraday probe acquisitions had a peak 11-12 kHz. It is possible that the presence of the probe subtly perturbed the thruster such that the breathing frequency decreased. In any case, the oscillation amplitude was comparable between diagnostics, and so it is suspected that the dynamics of the breathing mode are similar between these cases. However, this means that the data is most meaningfully presented as being a function of breathing phase rather than time. Most of the following figures will do this except where it is otherwise insightful.

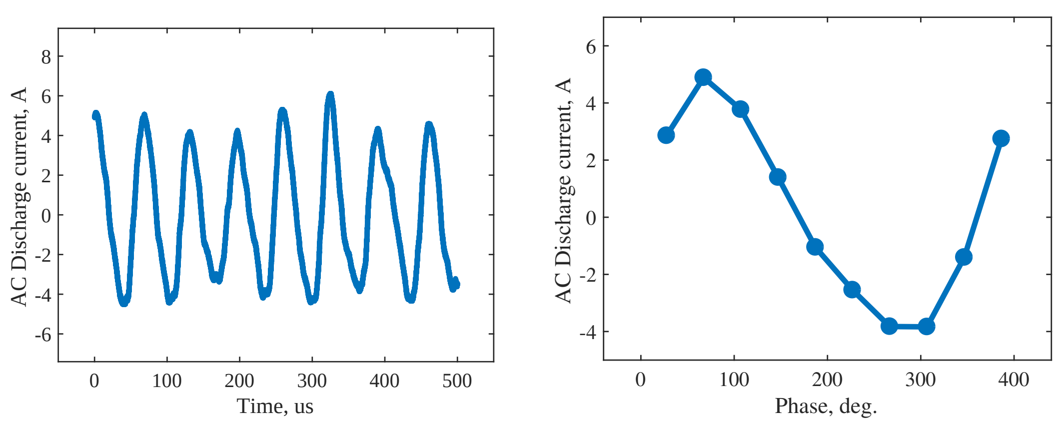

Fig. 6 A sample of the raw discharge current (left) and the boxcar-averaged signal (right). The discharge current has a vaguely sawtooth shape, which is captured in the averaged signal.

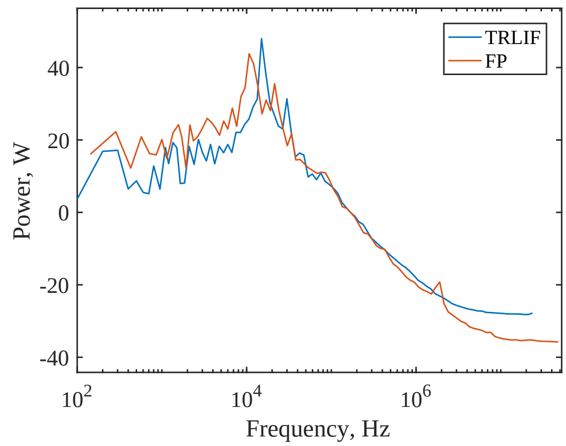

Fig. 7 The power spectrum of the discharge current is similar during Faraday probing and TRLIF but the peak frequency is slightly different. Additionally, the Faraday probe spectrum contains a high frequency peak absent in the TRLIF spectrum.

B. Local current density

Fig. 8 shows the measured Faraday probe current 35 mm downstream of the thruster exit plane, as well as the averaged signal. For context, the maximum possible current density at this operating condition is 57 mA/cm^2, so the values shown in Fig. 8 are physically reasonable. As expected, the beam current density correlates with the discharge current. By cross-correlating the raw data, it can be quantified that the beam current density lags the discharge current by roughly 102°. This agrees with the general notion in the literature that the breathing mode originates in the ionization region and convects downstream. However, it is anticipated that the ion transit time from the exit plane to the Faraday probe should be $\sim$10 μs for 300 V operation, producing a lag of 55° for a typical breathing cycle. This disparity will be reconsidered in further sections based on the LIF data collected in this study.

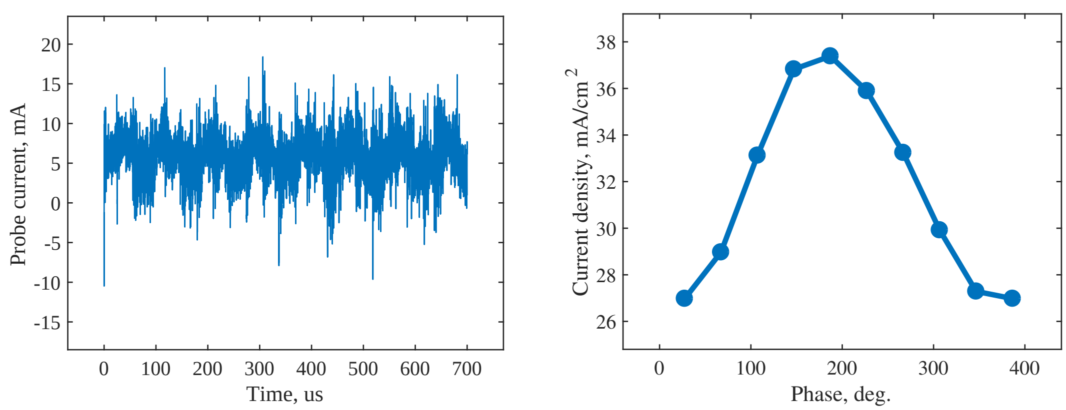

Fig. 8 The raw Faraday probe current (left) contains considerable noise while the corresponding averaged current density (right) is smooth and periodic at the breathing frequency.

C. Time-resolved IVDF Maps

Before discussing the entire time-resolved IVDF map measured as part of this experiment, it is important to show in detail what typical measured time-resolved IVDFs look like. This will shed light on some of the successes of the boxcar technique we used, and will also highlight some shortcomings anticipated in previous sections. Fig. 9 shows a series of time-resolved IVDFs acquired at the exit plane of the thruster. These traces are corrected for laser power but are unsmoothed. As they show, the SNR does indeed worsen at greater phases, and in general the SNR is poor. Fig. 9 is also an example of an IVDF cycle 3 mm upstream of the exit plane. The smearing discussed in Section V C is clearly present here, which suggests large-scale high-frequency fluctuations may be present in this region at those times. The high noise floor also acts to obscure the bottom of the "saddle", exaggerating the amount of smearing.

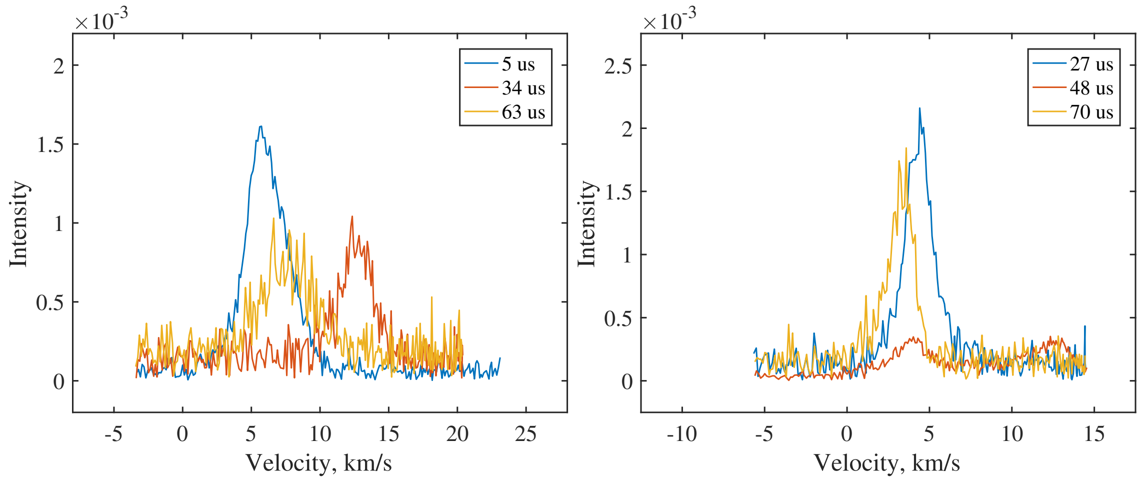

Fig. 9 The raw IVDF varies in time and generally becomes noisier for longer gate delays. Measured at the exit plane (left), the 34 and 63 μs IVDFs have roughly the same velocity extent and peak intensity, but the latter is observably noisier. Smeared IVDFs were measured at some locations in the TRLIF domain. The IVDF at -3 mm (right) is "clean" at 27 and 70 μs but has two peaks at 48 μs.

As an example of the multitude of IVDF maps acquired in this study, Fig. 10 shows a few maps at different times. As they clearly demonstrate, the ion population varies periodically on times scales corresponding to the breathing mode. Further, these plots show that far downstream the IVDF varies in mean velocity, while near the exit plane both the shape and mean of the distribution change. Far upstream, relatively little fluctuation is observable. However, it is interesting to note that toward 25 mm upstream, the peak velocity is nearly stationary, suggesting that this location is close to the anode pre-sheath edge, and thus it is not unexpected that this region is largely divorced from the downstream ion behavior.

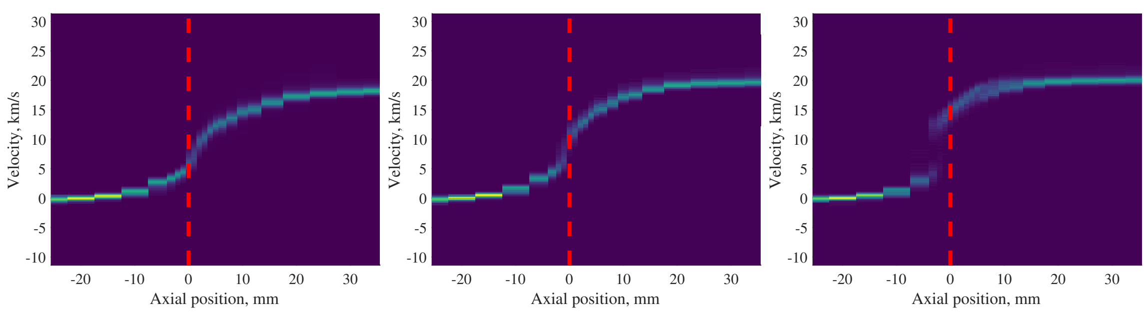

Fig. 10 The IVDF varies over a breathing cycle, with relatively little fluctuation from 28° (left) to 147° (middle), to a clear change in shape at 267° (right). Not only does the IVDF translate in velocity-space in the last sample above, it also steepens and there is a noticeable gap in the IVDF just upstream of the exit plane.

VII. Analysis

A. Boltzmann Quantities

We apply the technique described in Section IV to the data presented in the previous section to calculate electric field, ionization rate, and density. Although the last quantity is of primary interest in validating the 0D model described in Section III, insight can also be gained by examining the electric field and ionization rate. The moments of the IVDF had to be calculated at all spatial locations and times to apply the Boltzmann method. For example, Fig. 11 shows the mean velocity $\overline{u}$ as a function of time. As suspected from Fig. 10, the mean velocity fluctuates smoothly far upstream and far downstream but varies significantly near the exit plane, with a maximum peak-to-peak fluctuation of 42%. Judging by the rate at which the mean velocity changes, the acceleration region seems to be centered near the exit plane but moves back and forth. Additionally, since the slope of the mean velocity varies in time, it is likely the acceleration region width is fluctuating.

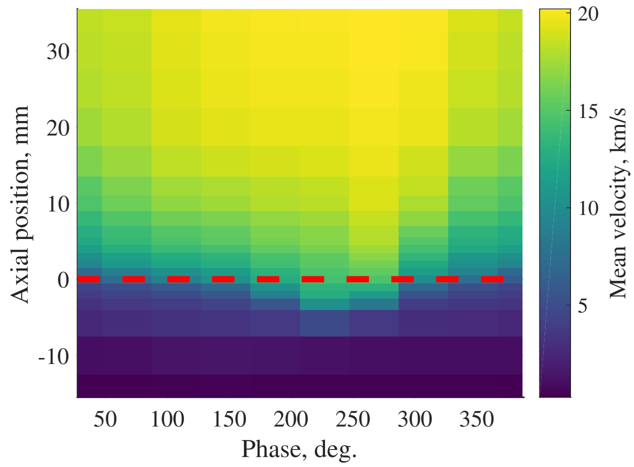

Fig. 11 The mean velocity $\overline{u}$ as a function of position and phase.

By applying the Boltzmann moment equations, Eqs. (13)-(15), using mean velocities like $\overline{u}$ shown in Fig. 11, we computed $\dot{n}_0$, $\partial n/\partial x$, and E. Since $\partial n/\partial x$ by itself is not particularly insightful, n is calculated from this quantity. Figure 12 shows the maps of computed density, electric field, and ionization rate. Note that these maps do not extend as far upstream as the TRLIF data: in this region the coarse spatial resolution of the IVDF measurements and the low mean velocities of these IVDFs make the density calculations unphysical. Also observe that the speculation of the acceleration region location and evolution based on Fig. 11 appears reasonable based on the upper right plot in Fig. 15.

B. Condition I: Correlation

The first observation presented at the end of Section III needed to validate the 0D model is correlation: density and ionization region width fluctuations must correlate with the discharge current. If this condition is not met, there is a fundamental disagreement between the 0D model and the experimental measurements, and likely this would be evidence that the measurements are flawed. To evaluate this condition, the ionization region must first be identified. The 0D model presumed that the ionization region would correspond with a peak in the ion density, but the upper left map of Fig. 12 shows the density monotonically increasing deep into the channel. Given that the acceleration region is near the exit plane according to the electric field map, and that the ionization region is likely near the acceleration region, it is improbably that the peak in ion density coincides with the ionization region.

Alternatively, the ionization region can be identified by the peak in ionization frequency, $\nu_{iz} \equiv dot n_0/n$, shown as the lower right map of Fig. 12. Figure 13 shows the evolution of the ionization and acceleration regions as a function of breathing phase. Determining the edges of these regions is somewhat arbitrary, but in this case we identified the them by finding where the middle 50% of the ionization frequency and electric field profiles are located. As may be expected based on the vague definition of the regions, Fig. 13 shows them overlapping significantly. Additionally, the width of the ionization region L_{iz} is periodic over a breathing cycle, and thus the ionization region width fluctuations correlate with breathing.

The variations in density over time are highlighted in Fig. 14, which shows the density normalized by its temporal mean at each location. The density fluctuations differ significantly over the spatial domain, but everywhere they are periodic over a breathing cycle, and thus density must also correlate with breathing. The first condition for validating the 0D model is therefore met according to the experimental data.

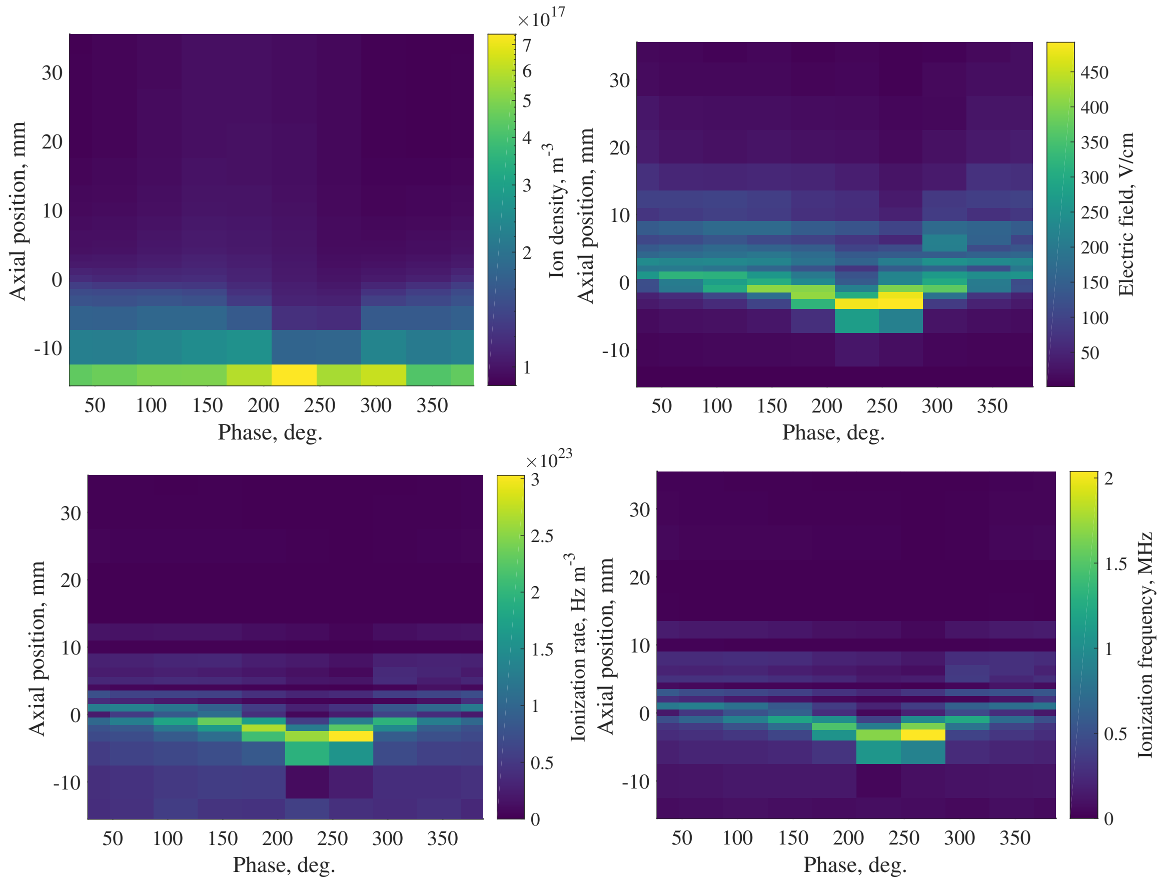

Fig. 12 The ion density (upper left), electric field (upper right), ionization rate (lower left), and ionization frequency (lower right) computed from the Boltzmann moments.

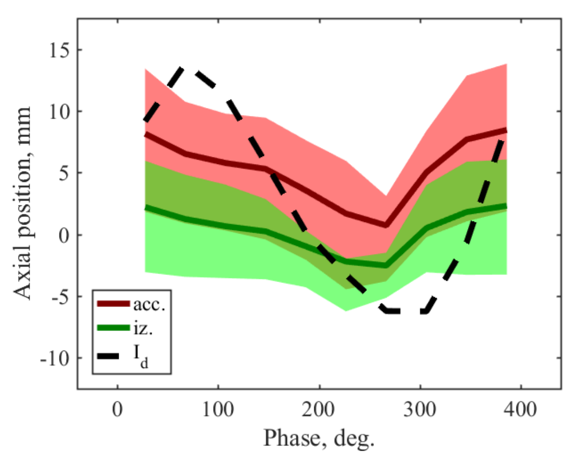

Fig. 13 The ionization and acceleration regions (left) can be identified as those areas containing some threshold percentage of acceleration/ionization. The two regions vary in width and location over a breathing cycle. The solid lines indicate the mean location of ionization/acceleration. The position of the mean within each region is indicative of the shape of the region. The discharge current signal is also shown for reference.

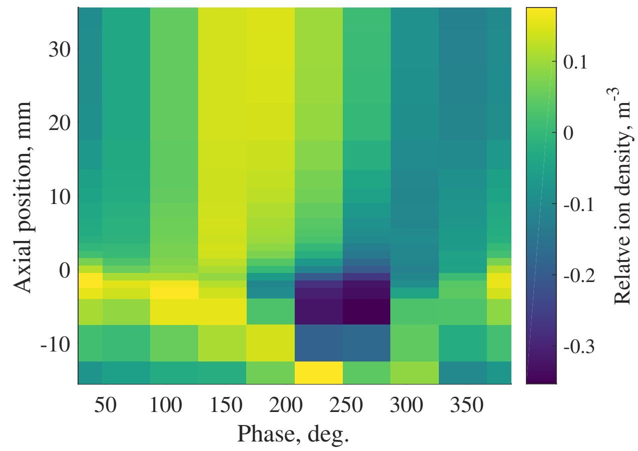

Fig. 14 The normalized density map, where fluctuations on the spatial mean are shown.

C. Condition II: Zero-dimensionality

The next condition to examine is whether the density fluctuates in phase throughout the ionization region. This is essentially a verification that the fluctuations are zero-dimensional, as the model fundamentally assumes. Since the definition of the ionization region from the experimental data is somewhat arbitrary, it is difficult to compare the density fluctuations across this entire region. However, the 0D model simply assumes that the fluctuations originate in the ionization region and convect downstream. So if we calculate the phase of these fluctuations over the whole domain, we can consider them zero-dimensional in nature if we observe an in-phase segment (convecting infinitely fast) near the ionization region, and a gradually lagging downstream segment(convecting at the ion beam speed). Figure 15 shows the density fluctuation phase lag profile compared to the discharge current signal. The density fluctuations can be computed in the laboratory frame as well as relative to the location of peak ionization frequency, and both are shown in Fig. 15. The latter assumes that the density fluctuations occur on top of the motion of the ionization region, as the 0D model arguably implicitly assumes. In any case, the lab frame profile shows a large in-phase segment encompassing the ionization region, while the other profile shows a singular point in phase with the discharge current signal. However, for both the phase lag increases suddenly downstream of 0 mm, equivalent to convection at roughly 200 m/s, which is far below the mean ion speed at this location. After this point, the fluctuations are convecting “infinitely fast", which likely means they are carried with the ion beam. Interestingly, both profiles also show convection toward the anode upstream of the in-phase region. In summary, regardless of the frame of reference there is an area downstream of the ionization region where the changes in phase are too slow to be explained by convection, which suggests that the fluctuations are evolving beyond the ionization region. So although the density fluctuations do correlate with discharge current, they are not entirely zero-dimensional. The zero-dimensionality condition is therefore not satisfied.

D. Condition III: Quadrature

The final condition to evaluate is whether the ionization region width L_{iz} lags behind the density fluctuations in the ionization region. We have already established that the fluctuations evolve outside this region, so for simplicity the density at the position of peak ionization frequency will be compared with the L_{iz}. This comparison is shown in Fig. 16, where all quantities are normalized. Density and L_{iz} appear to be out of phase, with the density peak leading by roughly 200°, and L_{iz} is approximately in phase with the discharge current. This means the quadrature condition may be met, although the poor temporal resolution makes it difficult to be certain. This data therefore suggests that the ionization region does vary during a breathing cycle and is capable of driving the instability. However, since the zero-dimensionality condition was not met, it is unclear whether the deformation of the ionization region realistically drives the instability.

E. Alternatives

Given that the conditions to validate the 0D model have not all been met, we are interested in looking for evidence of other possible sources for the instability. One avenue for exploring this is to consider the evolution of ion and electron current. Given that ion density and velocity are known everywhere, the ion current can be calculated assuming radial

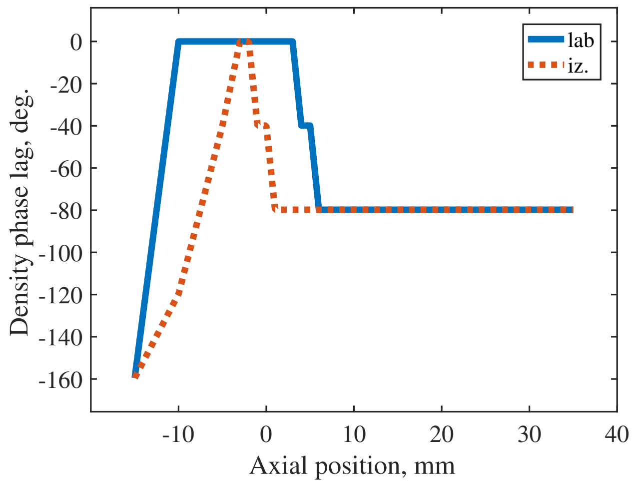

Fig. 15 The phase of density fluctuations in the laboratory frame (blue) and relative to the peak ionization frequency (red).

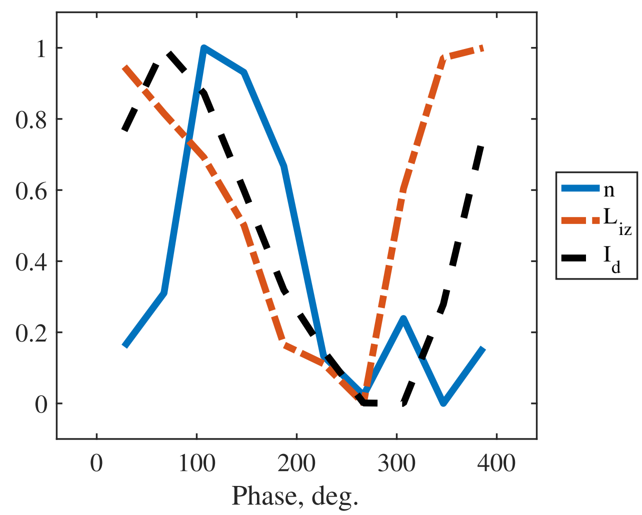

Fig. 16 Density at the location of peak ionization frequency is out of phase with the ionization region width, and the latter is roughly in phase with the discharge current.

uniformity. The radial distribution of current is probably not uniform in reality so the currents calculated here are more representative of radially-average current. To maintain current continuity, the difference in the total discharge current and the ion current must be the electron current. Therefore, even though this study focused on interrogating the ion population in the thruster, some electron information can also be deduced.

Fig. 17 shows the ion and electron current as a function of phase and position relative to the peak electric field (top), as well as the fluctuations in both (bottom). Unlike previous fluctuation maps, these values are not normalized. The electron current tends to be much larger than the ion current, and the electron current fluctuations are everywhere in phase and of similar amplitude. Both of these features could be a result of an underestimation of the ion current or neglect of conduction of current by other means. However, the H9's shielded magnetic field topography should focus much of plasma away from the channel walls, making these possibilities less likely. The electron current is in phase with the discharge current, while the ion current leads it. Additionally, the current fluctuations are mostly zero-dimensional in that they show little spatial variation upstream of the peak electric field. Moreover, the electrons do seem to play an important role given the magnitude of the fluctuation in electron current. Collectively, this suggests that a 0D description of the breathing mode will be more successful if it considers ion and electron current rather than ion density fluctuations alone.

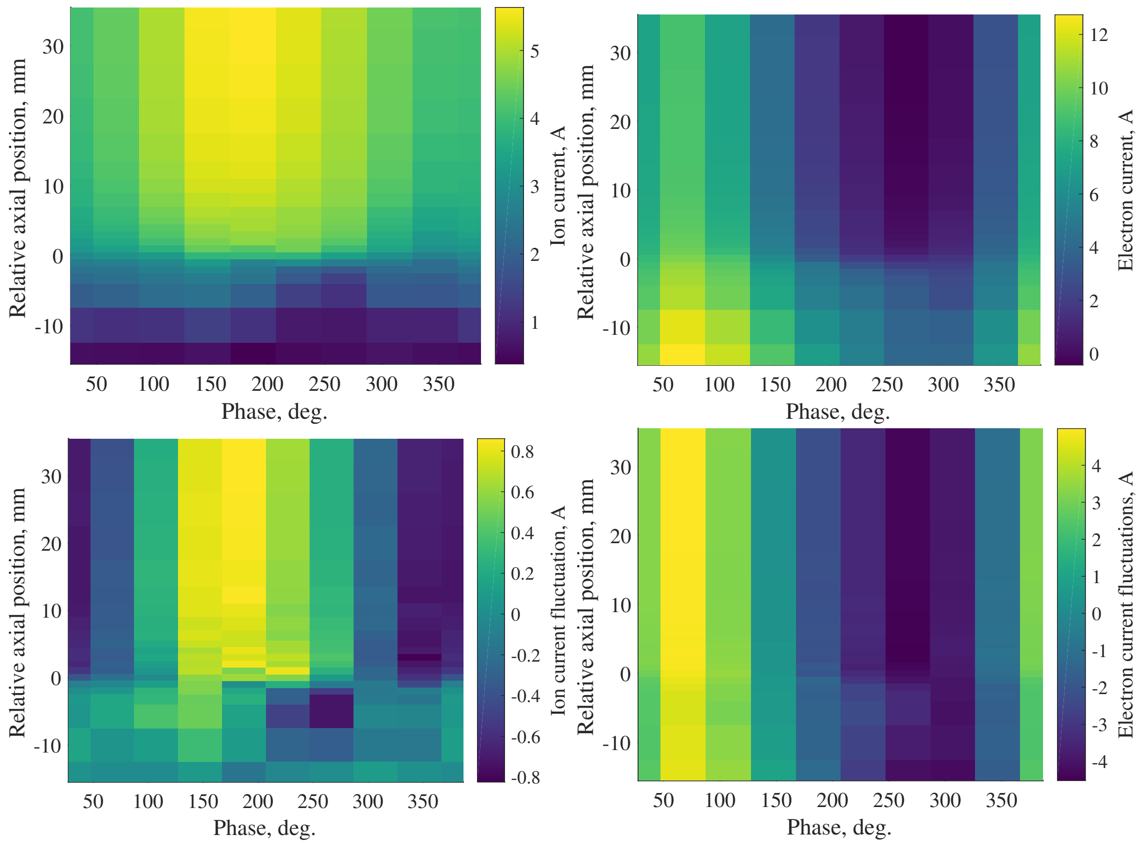

Fig. 17 The ion current (top left) and electron current (top right) can be calculated. The fluctuations (bottom left and bottom right, respectively) show different features than the density map.

VIII. Conclusions

The goal of this study was to use TRLIF to validate the physical assumption that deformation of the ionization region correlates with the breathing mode and that the growth of this mode can be ascribed to this effect. To do this, correlation, zero-dimensionality, and quadrature must be observed. A method for computing electric field, ionization rate, and ion density from time-resolved IVDF maps was developed to evaluate these conditions. The measurements showed that the first and third conditions were met but the second was not. The 0D model described in Section III may therefore not be physically realistic.

By comparing the evolution of ion and electron current during a breathing cycle, it becomes clear that these quantities fluctuate in a 0D fashion upstream of the peak electric field. Additionally, they are out of phase and thus are good candidates for a linear perturbation analysis. It is also interesting that the electron current fluctuations are consistent throughout the thruster and in general most of the discharge current is carried by the electrons. This suggests that electron dynamics are an important element of the breathing process.

Further extensions of the method used here to compute ion density, electric field, and ionization rate could be explored in future studies. It would be interesting to compare the Boltzmann values to those measured with electrostatic probes, although this would need to be done in a device less sensitive to the presence of probes. Beyond validation, this method could potentially be extended to computing certain electron properties if neutral density were known as well, perhaps via a different LIF scheme.

Acknowledgments

This work was supported by NASA Space Technology Fellowship NNX14AL65H. E. Dale would also like to thank Matthew Byrne for his assistance in carrying out the laser measurements discussed in this paper.

References

[1] Dale, E. T., Jorns, B., and Hara, K., "Numerical investigation of the stability criteria for the breathing mode in Hall Effect Thrusters," Atlanta, GA, 2017. URL https://iepc2017.org/sites/default/files/speaker-papers/iepc_2017_265.pdf.

[2] Oh, D. Y., Snyder, J. S., Goebel, D. M., Hofer, R. R., and Randolph, T. M., "Solar Electric Propulsion for Discovery-Class Missions," *Journal of Spacecraft and Rockets*, Vol. 51, No. 6, 2014, pp. 1822–1835. doi:10.2514/1.A32889, URL https://doi.org/10.2514/1.A32889.

[3] Choueiri, E. Y., "Plasma oscillations in Hall thrusters," *Physics of Plasmas (1994-present)*, Vol. 8, No. 4, 2001, pp. 1411–1426. doi:10.1063/1.1354644, URL http://scitation.aip.org/content/aip/journal/pop/8/4/10.1063/1.1354644.

[4] Sekerak, M. J., Gallimore, A. D., Brown, D. L., Hofer, R. R., and Polk, J. E., "Mode Transitions in Hall-Effect Thrusters Induced by Variable Magnetic Field Strength," *Journal of Propulsion and Power*, Vol. 32, No. 4, 2016, pp. 903–917. doi:10.2514/1.B35709, URL http://dx.doi.org/10.2514/1.B35709.

[5] Ortega, A. L., Mikellides, I. G., and Chaplin, V. H., "Numerical Simulations for the Assessment of Erosion in the 12.5-kW Hall Effect Rocket with Magnetic Shielding (HERMeS)," *35th International Electric Propulsion Conference, Atlanta, GA, IEPC-2017-154*, 2017.

[6] Tsikata, S., Heron, A., and Honore, C., "Oscillatory discharge behavior in Hall thrusters: relationships between the discharge current, electric feld and microturbulence," Atlanta, GA, 2017. URL https://iepc2017.org/sites/default/files/speaker-papers/manuscript_cts17.pdf.

[7] Fife, J., Martinez-Sanchez, M., and Szabo, J., "A numerical study of low-frequency discharge oscillations in Hall thrusters," *33rd AIAA/ASME/SAE/ASEE Joint Propulsion Conference and Exhibit*, American Institute of Aeronautics and Astronautics, 1997. doi:10.2514/6.1997-3052, URL http://arc.aiaa.org/doi/10.2514/6.1997-3052.

[8] Boeuf, J. P., and Garrigues, L., "Low frequency oscillations in a stationary plasma thruster," *Journal of Applied Physics*, Vol. 84, No. 7, 1998, pp. 3541–3554. doi:10.1063/1.368529, URL http://scitation.aip.org/content/aip/journal/jap/84/7/10.1063/1.368529.

[9] Parra, F. I., Ahedo, E., Fife, J. M., and Martínez-Sánchez, M., "A two-dimensional hybrid model of the Hall thruster discharge," *Journal of Applied Physics*, Vol. 100, No. 2, 2006, p. 023304. doi:10.1063/1.2219165, URL http://aip.scitation.org/doi/full/10.1063/1.2219165.

[10] Coche, P., and Garrigues, L., "A two-dimensional (azimuthal-axial) particle-in-cell model of a Hall thruster," *Physics of Plasmas*, Vol. 21, No. 2, 2014. doi:10.1063/1.4864625, URL http://aip.scitation.org/doi/abs/10.1063/1.4864625.

[11] Barral, S., and Peradzyński, Z., "Ionization oscillations in Hall accelerators," *Physics of Plasmas (1994-present)*, Vol. 17, No. 1, 2010. doi:10.1063/1.3292645, URL http://scitation.aip.org/content/aip/journal/pop/17/1/10.1063/1.3292645.

[12] Hara, K., "Development of Grid-Based Direct Kinetic Method and Hybrid Kinetic-Continuum Modeling of Hall Thruster Discharge Plasmas." Ph.D. thesis, University of Michigan, 2015. URL https://deepblue.lib.umich.edu/handle/2027.42/111379.

[13] Barral, S., and Ahedo, E., "Theoretical Study of the Breathing Mode in Hall Thrusters," *42nd AIAA/ASME/SAE/ASEE Joint Propulsion Conference & Exhibit*, American Institute of Aeronautics and Astronautics, Sacramento, CA, 2006. doi:10.2514/6.2006-5172, URL https://arc.aiaa.org/doi/abs/10.2514/6.2006-5172.

[14] Hara, K., Sekerak, M. J., Boyd, I. D., and Gallimore, A. D., "Perturbation analysis of ionization oscillations in Hall effect thrusters," *Physics of Plasmas (1994-present)*, Vol. 21, No. 12, 2014. doi:10.1063/1.4903843, URL http://scitation.aip.org/content/aip/journal/pop/21/12/10.1063/1.4903843.

[15] Barral, S., and Ahedo, E., "Low-frequency model of breathing oscillations in Hall discharges," *Physical Review E*, Vol. 79, No. 4, 2009. doi:10.1103/PhysRevE.79.046401, URL http://link.aps.org/doi/10.1103/PhysRevE.79.046401.

[16] Barral, S., and Ahedo, E., "On the Origin of Low Frequency Oscillations in Hall Thrusters," *AIP Conference Proceedings*, Vol. 993, AIP Publishing, 2008, pp. 439–442. doi:10.1063/1.2909170, URL http://scitation.aip.org/content/aip/proceeding/aipcp/10.1063/1.2909170.

[17] Hurwitz, A., "On the conditions under which an equation has only roots with negative real parts," *Selected papers on mathematical trends in control theory*, Vol. 65, 1964, pp. 273–284.

[18] Boeuf, J.-P., "Tutorial: Physics and modeling of Hall thrusters," *Journal of Applied Physics*, Vol. 121, No. 1, 2017. doi:10.1063/1.4972269, URL http://aip.scitation.org/doi/full/10.1063/1.4972269.

[19] Haas, J. M., "Low-perturbation interrogation of the internal and near-field plasma structure of a Hall thruster using a high-speed probe positioning system," Ph.D. thesis, US Air Force Research Laboratory, 2001. URL http://www.pepl.engin.umich.edu/pdf/2001_haas_thesis.pdf.

[20] Lobbia, R. B., and Gallimore, A. D., "High-speed dual Langmuir probe," *Review of Scientific Instruments*, Vol. 81, No. 7, 2010, p. 073503. doi:10.1063/1.3455201, URL http://scitation.aip.org/content/aip/journal/rsi/81/7/10.1063/1.3455201.

[21] Lobbia, R. B., "A Time-resolved Investigation of the Hall Thruster Breathing Mode," Ph.D. thesis, University of Michigan, Ann Arbor, MI, 2010. URL https://deepblue.lib.umich.edu/handle/2027.42/76022.

[22] Dale, E., Gallimore, A., and Lobbia, R., "Time-resolved internal Hall thruster plasma measurements using a high-speed Langmuir probe," Phoenix, AZ, 2016.

[23] Jorns, B., Goebel, D. M., and Hofer, R. R., "Plasma Perturbations in High-Speed Probing of Hall Thruster Discharge Chambers: Quantification and Mitigation," *51st AIAA/SAE/ASEE Joint Propulsion Conference and Exhibit*, American Institute of Aeronautics and Astronautics, Orlando, FL, 2015. URL http://arc.aiaa.org/doi/abs/10.2514/6.2015-4006.

[24] Grimaud, L., Pétin, A., Vaudolon, J., and Mazouffre, S., "Perturbations induced by electrostatic probe in the discharge of Hall thrusters," *Review of Scientific Instruments*, Vol. 87, No. 4, 2016, p. 043506. doi:10.1063/1.4945563, URL http://scitation.aip.org/content/aip/journal/rsi/87/4/10.1063/1.4945563.

[25] Mazouffre, S., "Laser-induced fluorescence diagnostics of the cross-field discharge of Hall thrusters," *Plasma Sources Science and Technology*, Vol. 22, No. 1, 2013, p. 013001. doi:10.1088/0963-0252/22/1/013001, URL http://stacks.iop.org/0963-0252/22/i=1/a=013001.

[26] Chaplin, V. H., Conversano, R. W., Lobbia, R. B., Lopez Ortega, A., Mikellides, I. G., Hofer, R. R., and Jorns, B. A., "Laser-Induced Fluorescence Measurements of the Acceleration Zone in the 12.5 kW HERMeS Hall Thruster," Atlanta, GA, 2017. URL https://iepc2017.org/sites/default/files/speaker-papers/iepc_2017_229.pdf.

[27] Lucca Fabris, A., Young, C. V., and Cappelli, M. A., "Time-resolved laser-induced fluorescence measurement of ion and neutral dynamics in a Hall thruster during ionization oscillations," *Journal of Applied Physics*, Vol. 118, No. 23, 2015. doi:10.1063/1.4937272, URL http://aip.scitation.org/doi/full/10.1063/1.4937272.

[28] MacDonald-Tenenbaum, N., Young, C. V., Fabris, A. L., Nakles, M., Hargus Jr, W., and Cappelli, M. A., "Time-Synchronized Continuous Wave Laser Induced Fluorescence Velocity Measurements of a 600 Watt Hall Thruster," *34th International Electric Propulsion Conference*, Air Force Research Lab Edwards AFB Aerospace Systems Directorate, Kobe, Japan, 2015. URL http://www.dtic.mil/docs/citations/ADA627200.

[29] Ohler, S., Gilchrist, B., and Gallimore, A., "Microwave plume measurements of an SPT-100 using xenon and a laboratory model SPT using krypton," *31st Joint Propulsion Conference and Exhibit*, American Institute of Aeronautics and Astronautics, San Diego, CA, 1995. doi:10.2514/6.1995-2931, URL https://arc.aiaa.org/doi/abs/10.2514/6.1995-2931.

[30] Pérez-Luna, J., Hagelaar, G. J. M., Garrigues, L., and Boeuf, J. P., "Method to obtain the electric field and the ionization frequency from laser induced fluorescence measurements," *Plasma Sources Science and Technology*, Vol. 18, No. 3, 2009, p. 034008. doi:10.1088/0963-0252/18/3/034008, URL http://stacks.iop.org/0963-0252/18/i=3/a=034008.

[31] Dankanich, J. W., Walker, M., Swiatek, M. W., and Yim, J. T., "Recommended Practice for Pressure Measurement and Calculation of Effective Pumping Speed in Electric Propulsion Testing," *Journal of Propulsion and Power*, Vol. 33, No. 3, 2017, pp. 668–680. doi:10.2514/1.B35478, URL https://arc.aiaa.org/doi/10.2514/1.B35478.

[32] Hofer, R., Cusson, S., Lobbia, R., and Gallimore, A., "The H9 Magnetically Shielded Hall Thruster," *35th International Electric Propulsion Conference*, Vol. IEPC- 2017- 232, 2017.

[33] Cusson, S., Hofer, R., Lobbia, R., Jorns, B., and Gallimore, A., "Performance of the H9 Magnetically Shielded Hall Thrusters," *35th International Electric Propulsion Conference*, Vol. IEPC-2017-239, 2017.

[34] Huang, W., Gallimore, A. D., and Hofer, R. R., "Neutral Flow Evolution in a Six-Kilowatt Hall Thruster," *Journal of Propulsion and Power*, Vol. 27, No. 3, 2011, pp. 553–563. doi:10.2514/1.B34048, URL http://arc.aiaa.org/doi/10.2514/1.B34048.

[35] Jorns, B., Dodson, C. A., Anderson, J. R., Goebel, D. M., Hofer, R. R., Sekerak, M. J., Ortega, A. L., and Mikellides, I. G., "Mechanisms for Pole Piece Erosion in a 6-kW Magnetically-Shielded Hall Thruster," *52nd AIAA/SAE/ASEE Joint Propulsion Conference and Exhibit*, American Institute of Aeronautics and Astronautics, 2016. doi:10.2514/6.2016-4839, URL `https://arc.aiaa.org/doi/abs/10.2514/6.2016-4839`.

[36] Mazouffre, S., Gawron, D., and Sadeghi, N., "A time-resolved laser induced fluorescence study on the ion velocity distribution function in a Hall thruster after a fast current disruption," *Physics of Plasmas*, Vol. 16, No. 4, 2009, p. 043504. doi:10.1063/1.3112704, URL `https://aip.scitation.org/doi/10.1063/1.3112704`.

[37] Rapp, D., and Englander-Golden, P., "Total Cross Sections for Ionization and Attachment in Gases by Electron Impact. I. Positive Ionization," *The Journal of Chemical Physics*, Vol. 43, No. 5, 1965, pp. 1464–1479. doi:10.1063/1.1696957, URL `https://aip.scitation.org/doi/abs/10.1063/1.1696957`.